Cross-plane thermoelectric transport in p-type La$_{0.67}$Sr$_{0.33}$MnO$_3$/LaMnO$_3$ oxide metal/semiconductor superlattices

Pankaj Jha,[1,2] Timothy D. Sands,[1,2,3,a)] Philip Jackson,[4] Cory Bomberger,[5] Tela Favaloro,[4] Stephen Hodson,[6] Joshua Zide,[5] Xianfan Xu,[6] and Ali Shakouri[1,2]

[1]*School of Electrical and Computer Engineering, Purdue University, West Lafayette, Indiana 47907, USA*
[2]*Birck Nanotechnology Center, Purdue University, West Lafayette, Indiana 47907, USA*
[3]*School of Materials Engineering, Purdue University, West Lafayette, Indiana 47907, USA*
[4]*Electrical Engineering Department, University of California, Santa Cruz, California 95064, USA*
[5]*Material Science and Engineering Department, University of Delaware, Newark, Delaware 19716, USA*
[6]*School of Mechanical Engineering and Birck Nanotechnology Center, Purdue University, West Lafayette, Indiana 47907, USA*

The cross-plane thermoelectric transport properties of La$_{0.67}$Sr$_{0.33}$MnO$_3$ (LSMO)/LaMnO$_3$ (LMO) oxide metal/semiconductor superlattices were investigated. The LSMO and LMO thin-film depositions were performed using pulsed laser deposition to achieve low resistivity constituent materials for LSMO/LMO superlattice heterostructures on (100)-strontium titanate substrates. X-ray diffraction and high-resolution reciprocal space mapping indicate that the superlattices are epitaxial and pseudomorphic. Cross-plane devices were fabricated by etching cylindrical pillar structures in superlattices using inductively, this coupled-plasma reactive-ion etching. The cross-plane electrical conductivity data for LSMO/LMO superlattices reveal a lowering of the effective barrier height to 223 meV as well as an increase in cross-plane conductivity by an order of magnitude compared to high resistivity superlattices. These results suggest that controlling the oxygen deficiency in the constituent materials enables modification of the effective barrier height and increases the cross-plane conductivity in oxide superlattices. The cross-plane LSMO/LMO superlattices showed a giant Seebeck coefficient of 2560 μV/K at 300 K that increases to 16 640 μV/K at 360 K. The giant increase in the Seebeck coefficient with temperature may include a collective contribution from the interplay of charge, spin current, and phonon drag. The low resistance oxide superlattices exhibited a room temperature cross-plane thermal conductivity of 0.92 W/m K, this indicating that the suppression of thermal conductivities due to the interfaces is preserved in both low and high resistivity superlattices. The high Seebeck coefficient, the order of magnitude improvement in cross-plane conductivity, and the low thermal conductivity in LSMO/LMO superlattices resulted in a two order of magnitude increase in cross-plane power factor and thermoelectric figure of merit (*ZT*), compared to the properties of superlattices with higher resistivity that were reported previously. The temperature dependence of the cross-plane power factor in low resistance superlattices suggests a direction for further investigations of the potential LSMO/LMO oxide superlattices for thermoelectric devices. © *2013 AIP Publishing LLC.*
[http://dx.doi.org/10.1063/1.4804937]

I. INTRODUCTION

Perovskite oxides display a rich variety of electronic properties as metals, ferroelectrics, ferromagnetics, multiferroics, and thermoelectrics. Due to their diverse range of properties, temperature stability, and robust chemistry, perovskite oxides have garnered interest from the scientific community for potential application as thermoelectric materials. Cross-plane electron filtering transport in metal/semiconductor superlattices provides a potential technique to increase the thermoelectric figure of merit (*ZT*).[1] The increase in the power factor from energy filtering is due to the expectation that a Schottky barrier will introduce a greater asymmetry in the differential conductivity about the Fermi level by cutting off the low energy tail. The reduction in transport carriers is compensated by a well with metallic level carrier concentration. The efficiency of a thermoelectric device is given by the dimensionless figure of merit, *ZT*; $ZT = \frac{S^2 \sigma}{(\kappa_e + \kappa_l)} T$, where *S* is the Seebeck coefficient, σ is the electrical conductivity, *T* is the absolute temperature (K), and κ is the thermal conductivity. P-type La$_{0.67}$Sr$_{0.33}$MnO$_3$ (LSMO)/LaMnO$_3$ (LMO) metal/semiconductor superlattices were deposited on (100)-strontium titanate (STO) substrates by pulsed laser deposition (PLD). The Schottky barrier height of LSMO/LMO superlattices calculated using band alignment ($\Phi_B = E_g + \chi_s - \Phi_m$) is 300 meV $\sim$ 11 kT at 300 K with closely matched lattice parameters.[2,3] The lowering of the barrier height of 11 kT in the valence band for p-type material enables an improvement of the power factor ($S^2 \sigma$) by filtering out the lower energy carriers, and the lattice-matched superlattices allow a reduction of the thermal conductivity.[4] Preliminary work focused

a)Author to whom correspondence should be addressed. Electronic mail: tsands@purdue.edu

on cross-plane transport of high resistivity p-type LSMO/ LMO superlattices. The high resistivity helped mitigate the effects of electrical and thermal parasitics in cross-plane transport measurements, thereby allowing interpretation of measurements of thermionic transport, barrier height, and lattice thermal conductivity. These high resistivity superlattices used for the prior investigation were grown at a low oxygen partial pressure of 50 ± 2 mTorr. The low oxygen partial pressure resulted in a film with in-plane resistivities more than two orders of magnitude higher than the resistivities obtained at higher oxygen partial pressure during growth.[5] LSMO/LMO superlattices exhibited a substantially lower room temperature thermal conductivity (0.89 W/m-K) than those of the constituent materials, which indicates that cross-plane phonon scattering reduces the lattice contribution to the thermal conductivity. The cross-plane conductivity of the superlattice structure extracted from I-V-T measurements of etched pillars suggests a contribution from thermionic behavior, and the extracted effective barrier height of 300 ± 15 meV is consistent with the theoretically expected LSMO/LMO Schottky barrier height (Φ_B) of ~ 300 meV at 300 K. The measured Seebeck coefficient was 1520 ± 53 μV/K. In spite of the suppressed thermal conductivity, the *ZT* achieved was low due to a low power factor ($S^2\sigma$), which was a consequence of the high resistivities of the constituent materials combined with a high barrier height relative to kT at room temperature.[6]

The present work focused on increasing the cross-plane conductivity in superlattices by using low resistivity constituent materials and by lowering the effective barrier height. In this paper, the deposited low resistivity heterostructures and their cross-plane thermoelectric transport properties are discussed in light of prior measurements of high-resistivity superlattices. The potential for tuning perovskite oxide superlattices for applications as thermoelectric materials at moderate temperatures is also evaluated.

II. EXPERIMENT

The growth of LSMO and LMO thin films on (100)-oriented cubic STO substrates was achieved using PLD. The growth conditions used were 248 nm KrF excimer laser (pulse width of 25 ns), laser fluence of 1.3 J/cm^2, pulse frequency of 5 Hz, and temperature maintained at 750 °C measured using an infrared pyrometer (STO emissivity of 0.8). The target was mechanically polished prior to each growth to achieve a uniform film. Epitaxial high resistivity thin films of LSMO and LMO on STO were also deposited by PLD using a background O$_2$ pressure of 52 mTorr to compare their post-growth annealing behavior with that of a sample grown at a higher oxygen partial pressure of 280 mTorr. Post-growth annealing in oxygen did not appreciably affect the conductivity of the sample grown at 52 mTorr (Fig. 1). Hence, the control of oxygen stoichiometry was focused on optimizing the oxygen partial pressure during growth to achieve low resistivity thin films and superlattices.

Optimization of the resistivity of the LSMO and LMO thin films was achieved with oxygen partial pressures in the
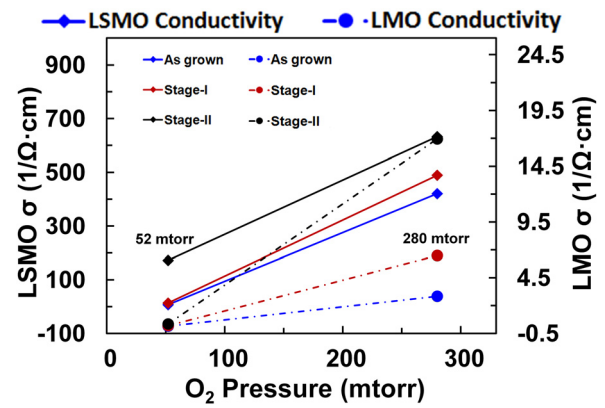

FIG. 1. Measured room temperature conductivity of LSMO and LMO thin films after two-stage annealing process: Stage-I (750 °C, 300 mTorr, 15 h PLD), and Stage-II (900 °C, atmospheric O$_2$ pressure, tube furnace).

range of 200–300 mTorr. The films grown at 210 ± 3 mTorr resulted in the lowest resistivity (Fig. 2). LSMO and LMO films were deposited under conditions that yielded a 100× increase in electrical conductivity compared to thin films at 52 mTorr, approaching the conductivity of a good thermoelectric material ($\sim 1000/\Omega$ cm). The oxygen partial pressure effect on conductivity can be related to double exchange interactions between Mn^{3+} and Mn^{4+} ions. The parent compound LaMnO$_3$ (Mn^{3+}, t$^3_{2g}$e^1_g), with ion vacancies of La^{3+}, Mn^{3+}, and O^{2-}, allows doping on all lattice sites. The parent compound exhibits a ferromagnetic and semiconducting phase and conducts by cation transitions.[7,8] The cation vacancies are responsible for causing mixed manganese Mn^{3+} and Mn^{4+} ions for charge neutrality.[9] LaMnO$_3$ with Sr^{2+} doping (La$_{0.67}$Sr$_{0.33}$MnO$_3$) creates a change of Mn^{3+} to Mn^{4+} with no e$_g$ electron (t$^3_{2g}$e^0_g). The hole hopping from a Mn^{4+} ion to a Mn^{3+} ion is possible only if the localized spins on adjacent Mn ions are parallel. This interaction between adjacent Mn ions is dominated by the double-exchange mechanism through an oxygen ion and is responsible for metallic behavior in LSMO.[10] These Mn^{4+} and Mn^{3+} ion concentrations are susceptible to any change in oxygen stoichiometry, which is controlled by the oxygen partial
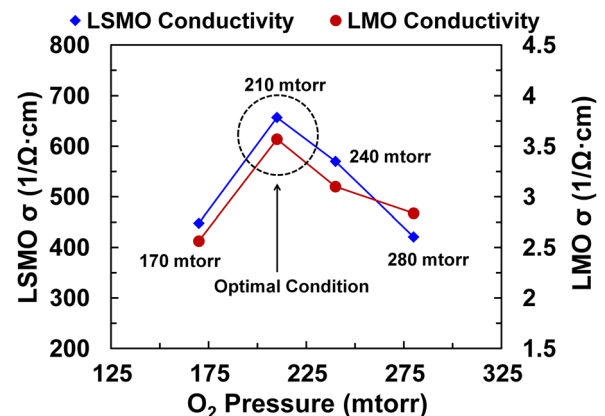

FIG. 2. Measured room temperature conductivity of the LSMO and LMO thin films grown at higher oxygen partial pressure. LSMO and LMO films were deposited under 210 mTorr that yielded a 100× increase in electrical conductivity compared to high resistivity constituent material thin films grown at 52 mTorr oxygen partial pressure.

pressure. A higher oxygen partial pressure increases the Mn^{4+} ion concentration, which results in higher conductivity and higher mobility. A lower oxygen partial pressure creates oxygen vacancies, which accommodate in the vicinity of Mn^{3+} ions compared to Mn^{4+} ions. For every oxygen vacancy, one Mn^{4+} is replaced by two Mn^{3+} ions with a significant increase in the c-axis lattice parameter in LMO, resulting in high resistivity films.[11–13] The LSMO and LMO samples grown at higher oxygen partial pressures have a high concentration of carriers, resulting in low resistivity films with better mobility.

LSMO and LMO thin-film structural analyses were performed using X-ray diffraction (XRD). XRD 2-theta-omega (2θ-ω) shows $\langle 001 \rangle$-textured LSMO films on STO substrates without any additional impurity phases. The narrow full-width-at-half-maximum (FWHM) intensity of the rocking curve ($0.012°$) suggests high crystalline quality. Highly aligned grains and in-plane epitaxy were confirmed by asymmetric 110 phi scans of LSMO on STO, which showed that all four $90°$-separated film peaks were well-aligned with the substrate peaks. LMO 2θ-ω analyses of the sample grown at a higher oxygen pressure in the range of 200–300 mTorr showed that the LMO peak at 3.89 Å overlaps with the STO substrate peak. In contrast, for LMO films grown at a low oxygen partial pressure of 52 mTorr, the c-axis lattice parameter increases from 3.89 Å to 3.94 Å (Fig. 3). The overlapping of the LMO film peak with the STO peak at higher oxygen partial pressure is consistent with prior observations.[12] 110 asymmetric phi scans confirmed highly aligned grains and in-plane epitaxy. Symmetrical 002 reciprocal space mapping (RSM) showed the LMO peak intensity spread overlaps with the high intensity STO peak, confirming epitaxy.

The low resistivity LSMO/LMO superlattices were grown at 210 ± 3 mTorr oxygen partial pressure, maintaining all other growth parameters the same (Fig. 4). The 2θ-ω analyses showed that the 002 film peak aligned with the STO 002 peak, confirming epitaxy (Fig. 5(a)). In-plane epitaxy and aligned grain were confirmed by asymmetric 110 phi

FIG. 4. Schematic of metallic LSMO (8 nm)/semiconducting LMO (8 nm) superlattice (LSMO/LMO)$_{51}$ structure grown by PLD.

FIG. 5. (a) XRD 2-theta-omega scan of an LSMO/LMO superlattice on a STO (100) substrate confirming c-axis epitaxial behavior with LSMO FWHM ($0.187°$) and (b) 110 RSM of a micron-thick LSMO/LMO superlattice confirming the LMO peak overlapping with STO peak, and pseudomorphic growth of epitaxial LSMO and LMO superlattice films.
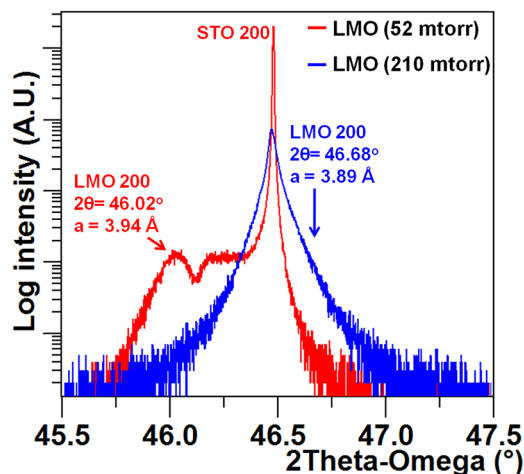

FIG. 3. XRD 2-theta-omega scan of an LMO on a STO (100) substrate confirming c-axis epitaxial behavior. The LMO grown at 52 mTorr partial oxygen pressure shows a distinguishing peak with a = 3.94 Å whereas the LMO grown at 210 mTorr peak overlaps with the STO peak.
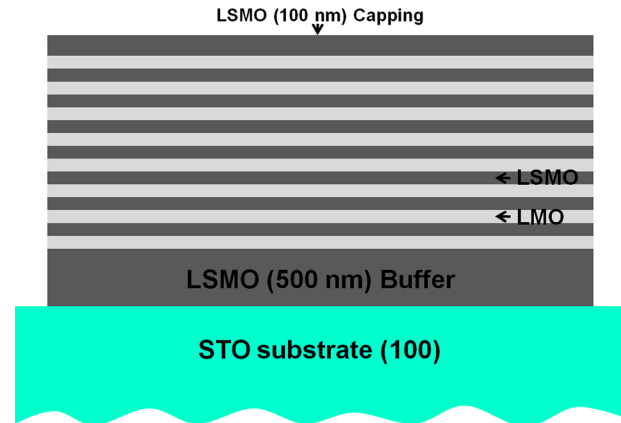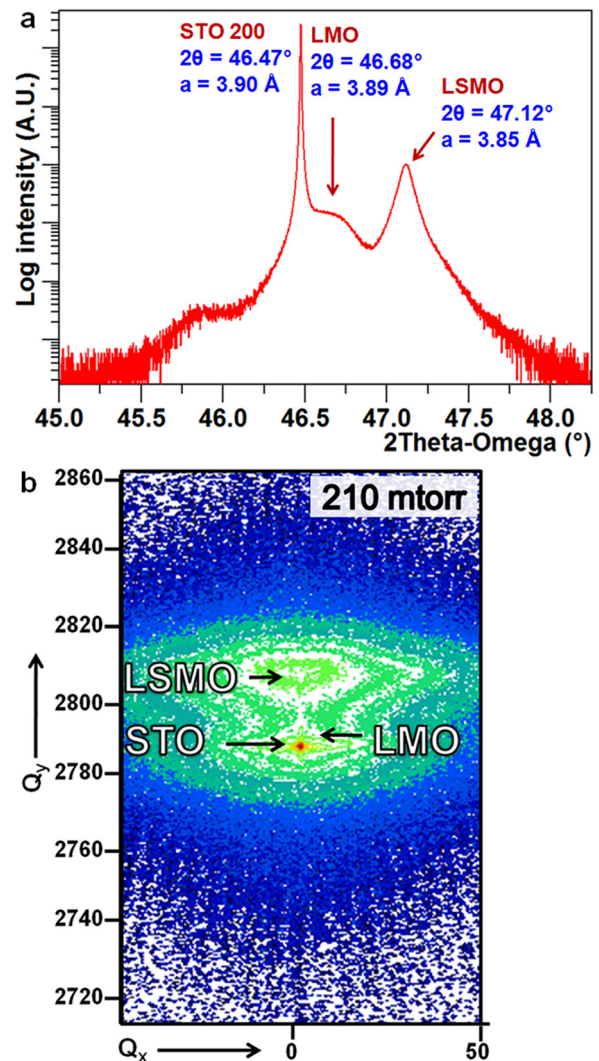
scans of superlattices, which showed that all four 90°-separated film peaks of LSMO and LMO were well-aligned with the STO substrate peaks. A 110 reciprocal space map from an oxide superlattice was analyzed to understand the degree of relaxation and strain in the superlattice layers (Fig. 5(b)). The degree of spread around the STO peak confirms that the LMO peak overlaps with the STO peak; this overlap along with the intense LSMO peak confirms the pseudomorphic nature of the superlattice on STO substrates.

III. RESULTS AND DISCUSSION

A. LSMO and LMO thin films

The in-plane electrical transport properties of epitaxial LSMO grown at 210 mTorr were extracted from measurements of resistivity, Seebeck coefficient, and carrier concentration. Hall measurements of a 200 nm thick epitaxial LSMO film on STO showed a room temperature resistivity of $1.52 \times 10^{-3}\,\Omega\,cm$, a hole carrier concentration of $1.12 \times 10^{21}\,cm^{-3}$, and mobility of $3.67\ cm^2/Vs$, in the range of typical oxide thermoelectric materials. Four-probe temperature dependent resistivity (TDR) measurements of LSMO, with ($H = 0.2\,T$) and without ($H = 0\,T$) a magnetic field, showed a $100\times$ increase in electrical conductivity compared to high resistivity LSMO thin films grown at 52 mTorr (Fig. 6(a)), approximately in the range of a good

thermoelectric material ($\sim 1000/\Omega\,cm$). The increase in the conductivity of LSMO is due to a higher carrier concentration with polaronic hopping conduction, with an extracted thermal activation energy (E_A) of 97.0 ± 5 meV.[14,15] The in-plane temperature dependent Seebeck measurement of LSMO showed a Seebeck coefficient with a magnitude less than $15\,\mu V/K$ over the entire temperature range, which is consistent with metallic behavior (Fig. 7(a)).[16]

Similarly, an epitaxial 200 nm thin film of LMO was characterized using the Hall effect measurement technique, which provided a room temperature resistivity of $2.79 \times 10^{-1}\,\Omega\,cm$, and a hole carrier concentration of $1.15 \times 10^{19}\,cm^{-3}$ with a hole mobility of $1.94\ cm^2/Vs$. Temperature dependent four-probe resistivity measurement of LMO with and without magnetic field also showed a $100\times$ increase in the conductivity, with a thermal activation energy (E_A) of 93.0 ± 5 meV (Fig. 6(b)). The in-plane temperature dependent Seebeck measurement with a room temperature Seebeck coefficient of $60 \pm 3\,\mu V/K$ confirmed that the LMO films were p-type (Fig. 7(b)).

The temperature dependent resistivity measurement at a magnetic field of 0.2 T of LSMO thin films grown at a higher oxygen pressure (210 mTorr) shows low magnetoresistance ($\sim 6\%$) and a LMO thin-film MR ratio of $\sim 40\%$. The LSMO sample grown at 52 mTorr showed a MR ratio of $\sim 16\%$ and the LMO MR ratio was $\sim 52\%$. This high MR in the sample grown at low oxygen pressure is attributed to a disordered
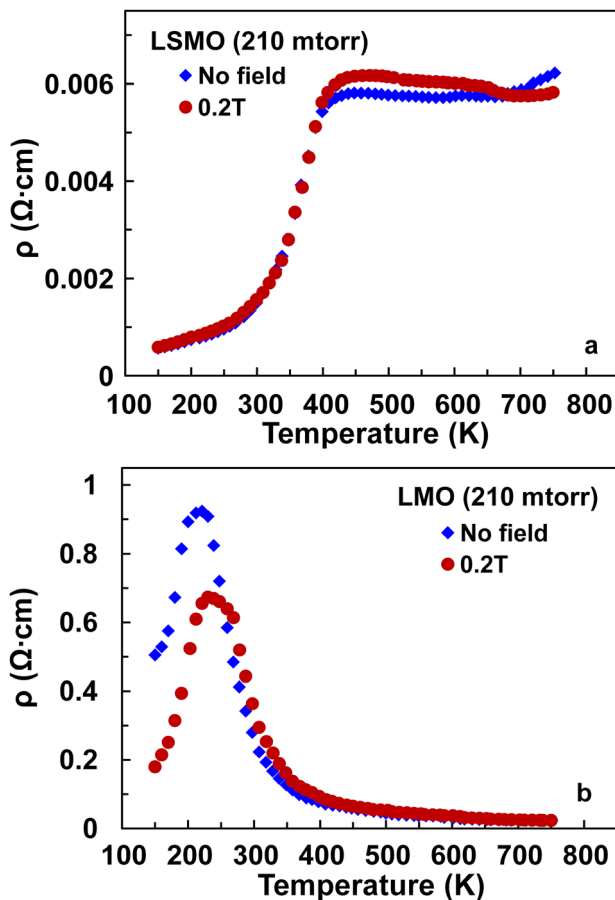

FIG. 6. Temperature-dependent in-plane resistivity with and without a magnetic field applied in a direction normal to the film surface for (a) LSMO, and (b) LMO.
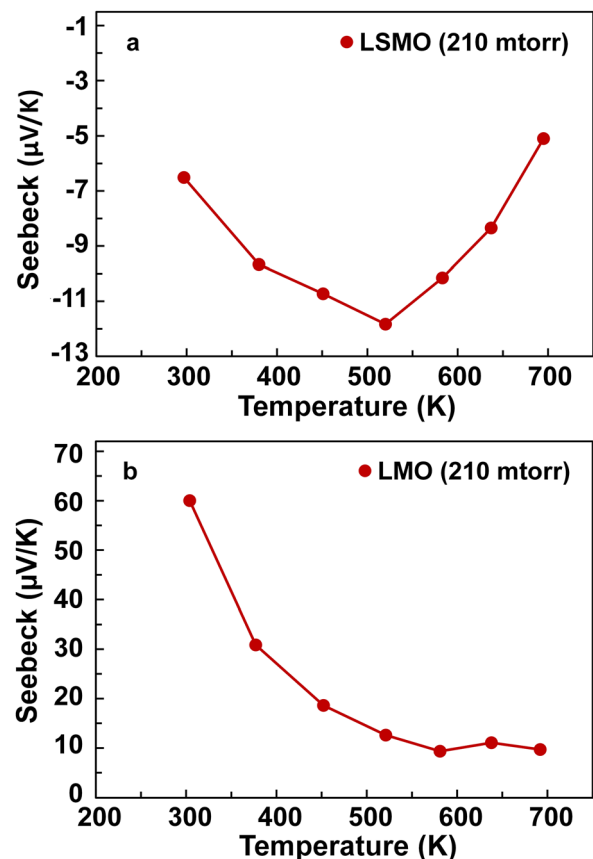

FIG. 7. (a) In-plane Seebeck measurement of LSMO showing that the Seebeck coefficient is consistent with metallic behavior with a magnitude of less than $15\,\mu V/K$ and (b) in-plane Seebeck measurement of LMO validating p-type behavior with a room temperature Seebeck coefficient of $60 \pm 3\,\mu V/K$.

spin state, in contrast to films grown at high oxygen pressure, which change to an ordered state with applied magnetic field.[11,17]

B. Cross-plane thermoelectric transport

Thermal conductivity of LSMO/LMO superlattices was measured using a photo-acoustic (PA) technique.[18,19] The high resistivity superlattices grown at 52 mTorr showed a cross-plane room temperature thermal conductivity of 0.89 W/m-K. Phonon scattering at interfaces showed a reduction in the lattice contribution to the thermal conductivity.[6] The low resistivity LSMO/LMO superlattices grown at 210 mTorr exhibited a room temperature thermal conductivity of 0.92 ± 0.12 W/m-K. The cross-plane thermal conductivity in the temperature range of 300 K–380 K is shown in Figure 8. The cross-plane thermal conductivity indicates that the suppression of thermal conductivity due to the interfaces is preserved. The estimated cross-plane electronic contribution (κ_e) using the Wiedemann-Franz law ($\kappa_e = L_o \sigma T$) was found to be negligible in both high and low resistivity LSMO/LMO superlattices. The measured temperature dependent thermal conductivity is comparably lower than that of bulk oxides and composite materials and comparable to heavy metallic alloys (0.5–2 W/m-K).[20]

The cross-plane electrical transport (power factor) measurement required etching of cylindrical pillar structures (1.1 μm height and 300 μm diameter) on the superlattices to reach the bottom buffer layer (Fig. 9(a)). The cylindrical pillar device structures were fabricated using AZ-9260 resist as an etching mask for inductively coupled plasma reactive ion etching (ICP-RIE) (Fig. 9(b)). The etching recipe used was 40:10 sccm of Cl_2:Ar, a chamber pressure of 0.7 Pa, a RF forward power of 800 W, and a capacitive bias of 350 W. The metallization used for top and bottom contacts consisted of three layers, Ti (8 nm)/Pt (125 nm)/Au (500 nm), to achieve good ohmic contact with LSMO/LMO superlattices. In-plane temperature-dependent resistivity measurements were performed on the LSMO/LMO superlattices (Fig. 10), which showed a thermal activation energy (E_A) of 114 ± 6 meV (Fig. 11). Temperature dependent I-V measurements in the temperature range of 100–600 K were
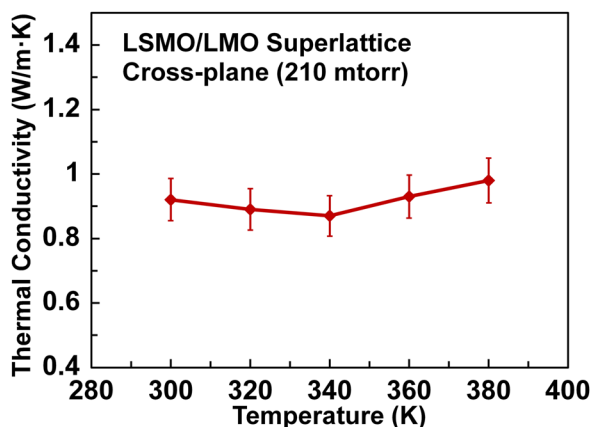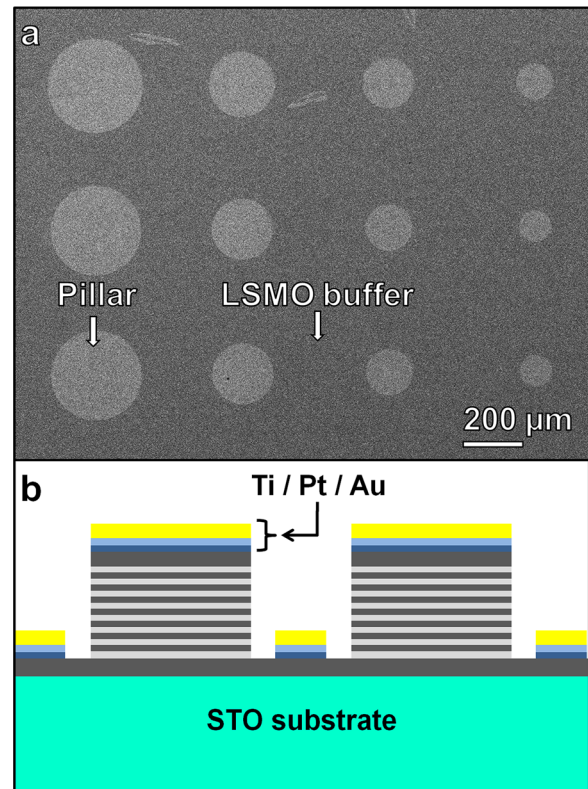

FIG. 9. (a) Field emission scanning electron microscope top view images of anisotropically etched LSMO/LMO superlattices by ICP-RIE, and (b) the schematic of side view of the final structure of LSMO/LMO superlattices for I-V cross-plane measurement.

performed on the cross-plane cylindrical devices. The extracted temperature dependent conductivity showed an order of magnitude increase in the cross-plane conductivity, compared to high resistivity superlattices (Fig. 12). The effective barrier height of 223 ± 11 meV was extracted from the cross-plane temperature dependent electrical conductivity data for LSMO/LMO superlattices (Fig. 13). The fact that the effective cross-plane barrier is higher than that measured for in-plane transport suggests that the temperature dependence of cross-plane conductivity was dominated by interface effects such as thermionic emission over interfacial barriers.

FIG. 8. Temperature-dependent cross-plane thermal conductivity of p-type LSMO/LMO superlattice.
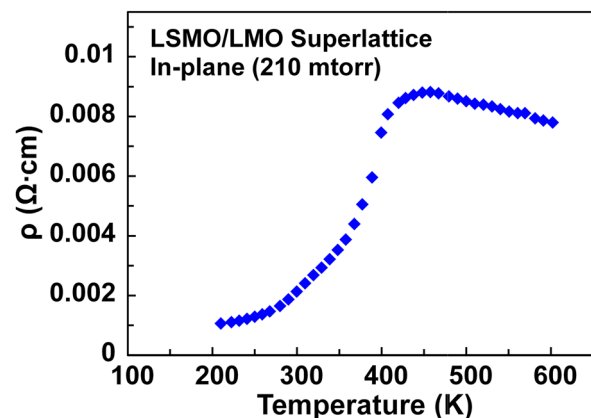

FIG. 10. Temperature-dependent in-plane resistivity of p-type LSMO/LMO superlattice.
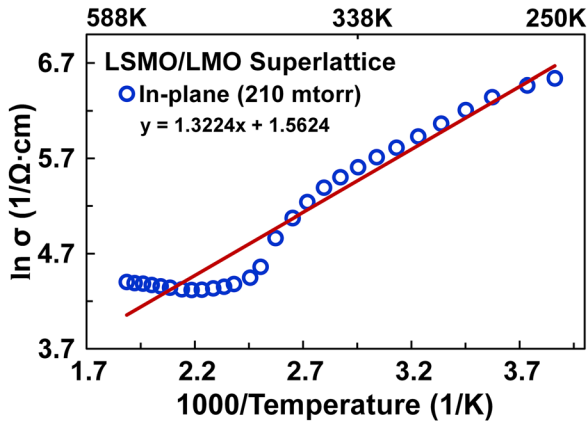
FIG. 11. The in-plane LSMO/LMO superlattice electrical conductivity plot fitted to extract the effective thermal activation energy of 114 ± 6 meV.
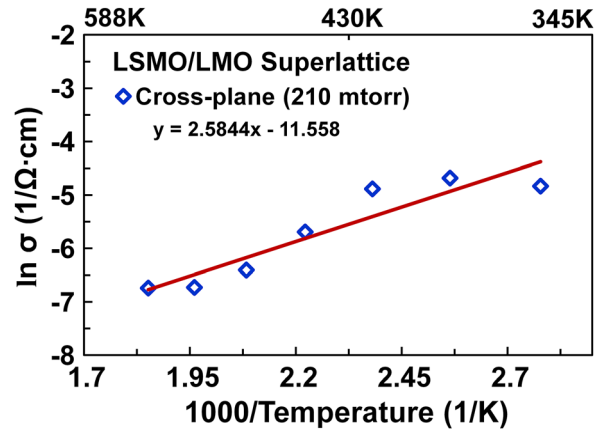

FIG. 13. Arrhenius plot of cross-plane LSMO/LMO superlattice electrical conductivity. The fitting extracted an effective barrier height of 223 ± 11 meV.

The modification of the room temperature barrier (Φ_B) height by varying the doping levels (i.e., by growing at high oxygen pressure) of the constituent materials in the superlattices enables the lowering of the effective barrier by approximately 75 meV.

Cross-plane Seebeck coefficient measurements in the temperature range of 300 K–360 K were performed using a thermal imaging technique.[21] The measured room temperature cross-plane Seebeck coefficient for low resistivity superlattices was $2560 \pm 130\ \mu$V/K. The Seebeck coefficient of the low resistivity sample increased with temperature to $8520 \pm 430\ \mu$V/K (320 K), $11\,160 \pm 560\ \mu$V/K (340 K), and $16\,640 \pm 830\ \mu$V/K (360 K) (Fig. 14). A "colossal" Seebeck coefficient of $\sim -45\,000\ \mu$V/K was reported by Bentien *et al.* in a strongly correlated semiconductor material ($FeSb_2$) with a very large thermal conductivity, which yielded a low thermoelectric figure of merit of 0.005°.[22–24] Later, Song *et al.* reported a "giant" Seebeck coefficient of $\sim -20\,000\ \mu$V/K in nano-MnO_2 powder sample around room temperature with a very high electrical resistance of 30 kΩ.[25] The measured Seebeck coefficient of low resistivity LSMO/LMO superlattices is higher, the cross-plane conductivity is higher, and the effective barrier is lower (by $\sim$75 meV) in comparison with

prior results with high resistivity superlattices. Although a lower barrier height (expressed as a ratio with k_BT) may yield a power factor that is closer to the optimal value in the thermionic model,[26] LSMO/LMO materials exhibit additional physics that may be at least as important in determining the cross-plane transport properties. The LSMO/LMO superlattice constituent materials exhibit spintronic properties where charges and spin current are intertwined and can generate a spin-Seebeck effect.[27,28] Therefore, the observed giant increase in the Seebeck coefficient with temperature in LSMO/LMO superlattices may be an indication of possible collective contribution from interplay of charge and spin transport in superlattices.[29–31] It may be concluded that the temperature gradient across the ferromagnetic conductor (LSMO) generates spin current. These spin currents may be injected into the ferromagnetic semiconductor (LMO) due to lowering of the effective barrier height, which leads to a giant spin-Seebeck effect. This phenomenon of generation of charge, spin current, and phonon-magnon (spin waves) coupling is referred to as the spin-Seebeck effect or spin calorit-ronic effect.[32–34] The entire contribution in the LSMO/LMO
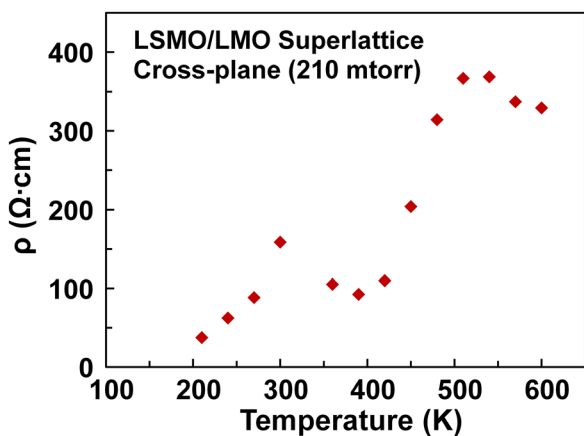

FIG. 12. Extracted cross-plane resistivity of the p-type LSMO/LMO superlattice using temperature dependent I-V measurement.
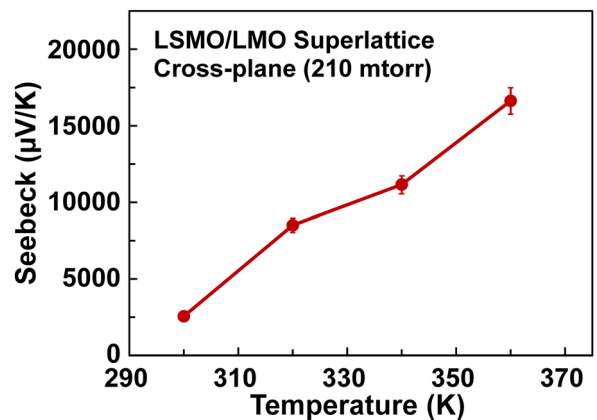

FIG. 14. The LSMO/LMO superlattice cross-plane Seebeck coefficient measurement using thermal imaging technique showed a giant Seebeck coefficient of $2560 \pm 130\ \mu$V/K at 300 K, which increased to $16\,640 \pm 830\ \mu$V/K at 360 K.
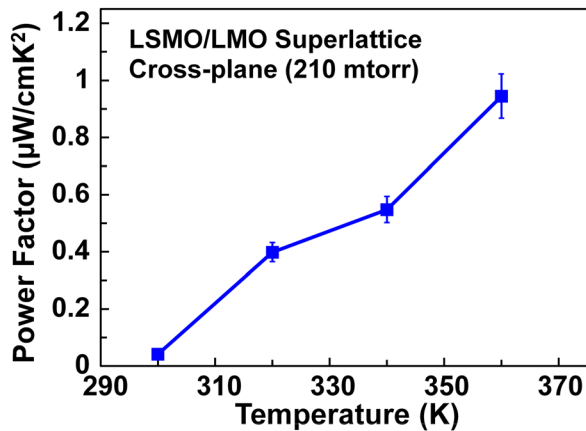
FIG. 15. The extracted cross-plane power factor ($S^2\sigma$) of the low resistivity p-type LSMO/LMO superlattice. The power factor increased by two orders of magnitude compared to high resistivity superlattices grown at 52 mTorr.

superlattice thermal conductivity is from the lattice contribution. Therefore, it may be possible that phonon-drag effects also contributed to the huge enhancement of the Seebeck coefficient in superlattices.[35] The giant contribution of spin-Seebeck, the large temperature dependence, and the low thermal conductivity in LSMO/LMO superlattices may offer opportunities to realize spin-dependent thermoelectric devices or magnetic thermoelectric devices where the collective effect of charge, spin, and heat transport can be utilized to increase the efficiency of thermoelectric devices.[36,37]

The extracted cross-plane temperature dependent power factor ($S^2\sigma$) of low resistivity LSMO/LMO superlattices (Fig. 15) increased by two orders of magnitude compared to high resistivity 52 mTorr superlattices and reached $\sim$0.95 μW/cm K^2. Combining the cross-plane power factor and thermal conductivity of the LSMO/LMO superlattices yielded a thermoelectric figure of merit (ZT) of $\sim$0.037 at 360 K (Fig. 16). Although this value is far from the range of useful values for power conversion (1.0 or greater), the increase of ZT by two orders of magnitude over that achieved for superlattices grown at 52 mTorr suggests that there is further room for improvement.
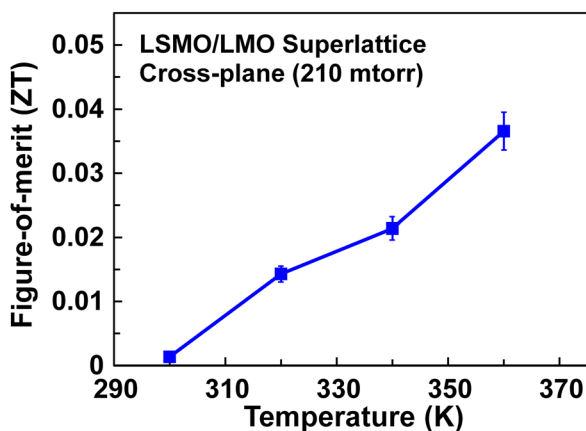

FIG. 16. The extracted cross-plane thermoelectric figure-of-merit (ZT) of p-type LSMO/LMO superlattices. The cross-plane ZT increased by two orders of magnitude compared to high resistivity superlattices grown at 52 mTorr.

IV. CONCLUSIONS

The increase in the power factor and ZT by two orders of magnitude for LSMO/LMO superlattices grown under conditions that yield constituent phases with low in-plane resistivities suggests that further modifications of these materials may lead to significant enhancements in thermoelectric transport properties. The results are consistent with on-going in-plane thermoelectric studies in perovskite oxide materials.[38,39] The current results suggest that the approach of using oxide superlattices may be a viable route toward a potential material for thermoelectric devices as a result of the low cross-plane thermal conductivity and the unusual physics that leads to the giant value of the Seebeck coefficient; however, much more work needs to be done to firmly establish oxide superlattices as a prospect for devices that operate at moderate and high temperature. The possibility to further increase cross-plane conductivity via doping/substitution of atoms, lowering of the effective barrier, and post-growth oxygen annealing of low resistivity superlattices may improve the thermoelectric figure of merit. The results of further studies should also elucidate the complex physics of transport in these artificial materials.

ACKNOWLEDGMENTS

[1]A. Shakouri and J. E. Bowers, "Heterostructure integrated thermionic coolers," Appl. Phys. Lett. **71**, 9 (1997).

[2]A. Urushibara, Y. Moritomo, T. Arima, A. Asamitsu, G. Kido, and Y. Tokura, "Insulator-metal transition and giant magnetoresistance in La$_{1-x}$Sr$_x$MnO$_3$," Phys. Rev. B **51**(20), 14103 (1995).

[3]T. Kida, G. Q. Guan, and A. Yoshida, "LaMnO$_3$/CdS nanocomposite: A new photocatalyst for hydrogen production from water under visible light irradiation," Chem. Phys. Lett. **371**, 563 (2003).

[4]R. Venkatasubramanian, "Lattice thermal conductivity reduction and phonon localization-like behavior in superlattice structures," Phys. Rev. B **61**(4), 3091 (2000).

[5]M. Huijben, L. W. Martin, Y. H. Chu, M. B. Holcomb, P. Yu, G. Rijnders, D. H. A. Blank, and R. Ramesh, "Critical thickness and orbital ordering in ultrathin La$_{0.7}$Sr$_{0.3}$MnO$_3$ films," Phys. Rev. B **78**, 094413 (2008).

[6]P. Jha, T. Sands, L. Cassels, P. Jackson, T. Favaloro, B. Kirk, X. Xu, J. Zide, and A. Shakouri, "Cross-plane electronic and thermal transport properties of p-type La$_{0.67}$Sr$_{0.33}$MnO$_3$/LaMnO$_3$ perovskite oxide metal/semiconductor superlattices," J. Appl. Phys. **112**, 063714 (2012).

[7]C. Aruta, M. Angeloni, G. Balestrino, N. G. Boggio, P. G. Medaglia, A. Tebano, B. Davidson, M. Baldini, D. Di Castro, P. Postorino, P. Dore, A. Sidorenko, G. Allodi, and R. De Renzi, "Preparation and characterization of LaMnO$_3$ thin films grown by pulsed laser deposition," J. Appl. Phys. **100**(2), 023910 (2006).

[8]A. Gupta, T. McGuire, P. Duncombe, M. Rupp, J. Sun, W. Gallagher, and G. Xiao, "Growth and giant magnetoresistance properties of La deficient La$_x$MnO$_{3-\delta}$(0.67 $\leq$ x $\leq$ 1) films," Appl. Phys. Lett. **67**, 3494 (1995).

[9]W. S. Choi, Z. Marton, S. Y. Jang, S. J. Moon, B. C. Jeon, J. H. Shin, S. S. A. Seo, T. W. Noh, K. Myung-Whun, H. N. Lee, and Y. S. Lee, "Effects of oxygen-reducing atmosphere annealing on LaMnO$_3$ epitaxial thin films," J. Phys. D: Appl. Phys. **42**(16), 165401 (2009).

[10]C. Zener, "Interaction between the d-shells in the transition metals. 2. Ferromagnetic compounds of manganese with perovskite structure," Phys. Rev. **82**(3), 403 (1951).

[11]J. Dho, N. Hur, I. Kim, and Y. Park, "Oxygen pressure and thickness dependent lattice strain in La$_{0.7}$Sr$_{0.3}$MnO$_3$ films," J. Appl. Phys. **94**, 7670 (2003).

[12]P. Orgiani, C. Aruta, R. Ciancio, A. Galdi, and L. Maritato, "Enhanced transport properties in La$_x$MnO$_{3-\delta}$ thin films epitaxially grown on SrTiO$_3$

substrates: The profound impact of the oxygen content," Appl. Phys. Lett. **95**, 013510 (2009).

[13]Y. S. Du, B. Wang, T. Li, D. B. Yu, and H. Yan, "Effects of annealing procedures on the structural and magnetic properties of epitaxial $La_{0.7}Sr_{0.3}MnO_3$ films," J. Magn. Magn. Mater. **297**, 88 (2006).

[14]J. Millis, P. B. Littlewood, and B. I. Shraiman, "Double exchange alone does not explain the resistivity of $La_{1-x}Sr_xMnO_3$," Phys. Rev. Lett. **74**, 5144 (1995).

[15]M. Ziese and C. Srinitiwarawong, "Polaronic effects on the resistivity of manganite thin films," Phys. Rev. B **58**, 11519 (1998).

[16]T. M. Palstra, A. P. Ramirez, S. W. Cheong, B. R. Zegarski, P. Schiffer, and J. Zaanen, "Transport mechanisms in doped $LaMnO_3$: Evidence for polaron formation," Phys. Rev. B **56**, 5104 (1997).

[17]P. Murugavel, P. Padhan, and W. Prellier, "Effect of oxygen pressure on the interface related magnetic and transport properties of $La_{0.7}Sr_{0.3}MnO_3/BaTiO_3$ superlattices," J. Phys.: Condens. Matter **18**, 3377 (2006).

[18]H. P. Hu, X. W. Wang, and X. F. Xu, "Generalized theory of the photoacoustic effect in a multilayer material," J. Appl. Phys. **86**(7), 3953 (1999).

[19]X. W. Wang, H. P. Hu, and X. F. Xu, "Photo-acoustic measurement of thermal conductivity of thin films and bulk materials," ASME Trans. J. Heat Transfer **123**(1), 138 (2001).

[20]H. Ohta, S. Kim, Y. Mune, T. Mizoguchi, K. Nomura, S. Ohta, T. Nomura, Y. Nakanishi, Y. Ikuhara, M. Hirano, H. Hosono, and K. Koumoto, "Giant thermoelectric Seebeck coefficient of two-dimensional electron gas in $SrTiO_3$," Nature Mater. **6**, 2 (2007).

[21]J. Christofferson and A. Shakouri, "Thermoreflectance based thermal microscope," Rev. Sci. Instrum. **76**(2), 024903 (2005).

[22]Bentien, S. Johnsen, G. Madsen, B. Iversen, and F. Steglich, "Colossal Seebeck coefficient in strongly correlated semiconductor $FeSb_2$," Europhys. Lett. **80**, 17008 (2007).

[23]D. Singh and I. Terasaki, "Thermoelectrics: Nanostructuring and more," Nature Mater. **7**, 616 (2008).

[24]Q. Jie, R. Hu, E. Bozin, A. Llober, I. Zalizyak, C. Petrovic, and Q. Li, "Electronic thermoelectric power factor and metal-insulator transition in $FeSb_2$," Phys. Rev. B **86**, 115121 (2012).

[25]F. Song, L. Wu, and S. Liang, "Giant Seebeck coefficient thermoelectric device of MnO_2 powder," Nanotechnology **23**, 085401 (2012).

[26]D. Vashaee and A. Shakouri, "Improved thermoelectric power factor in metal-based superlattices," Phys. Rev. Lett. **92**(10), 106103 (2004).

[27]K. Uchida, T. Ota, H. Adachi, J. Xiao, T. Nonaka, Y. Kajiwara, G. E. W. Bauer, S. Maekawa, and E. Saitoh, "Thermal spin pumping and magnon-phonon-mediated spin-Seebeck effect," J. Appl. Phys. **111**, 103903 (2012).

[28]K. Uchida, S. Takahashi, K. Harii, J. Ieda, W. Koshibae, K. Ando, S. Maekawa, and E. Saitoh, "Observation of the spin Seebeck effect," Nature **455**, 778 (2008).

[29]C. M. Jaworski, J. Yang, S. Mack, D. D. Awschalom, J. P. Heremans, and R. C. Myers, "Observation of the spin-Seebeck effect in a ferromagnetic semiconductor," Nature Mater. **9**, 898 (2010).

[30]K. Uchida, J. Xiao, H. Adachi, J. Ohe, S. Takahashi, J. Ieda, T. Ota, Y. Kajiwara, H. Umezawa, H. Kawai, G. E. W. Bauer, S. Maekawa, and E. Saitoh, "Spin Seebeck insulator," Nature Mater. **9**, 894 (2010).

[31]L. Gravier, S. Guisan, F. Reuse, and J. Ansermet, "Spin-dependent Peltier effect of perpendicular currents in multilayered nanowires," Phys. Rev. B **73**, 052410 (2006).

[32]A. Slachter, F. Bakker, J. Adam, and B. Wees, "Thermally driven spin injection from a ferromagnet into a non-magnetic metal," Nat. Phys. **6**, 879 (2010).

[33]F. Bakker, A. Slachter, J. Adam, and B. Wees, "Interplay of Peltier and Seebeck effects in nanoscale nonlocal spin valves," Phys. Rev. Lett. **105**, 136601 (2010).

[34]J. Breton, S. Sharma, H. Saito, S. Yuasa, and R. Jansen, "Thermal spin current from a ferromagnet to silicon by Seebeck spin tunneling," Nature **475**, 82 (2011).

[35]H. Adachi, K. Uchida, E. Saitoh, J. Ohe, S. Takahashi, and S. Maekawa, "Gigantic enhancement of spin Seebeck effect by phonon drag," Appl. Phys. Lett. **97**, 252506 (2010).

[36]C. M. Jaworski, J. Yang, S. Mack, D. D. Awschalom, R. C. Myers, and J. P. Heremans, "Spin-Seebeck effect: A phonon driven spin distribution," Phys. Rev. Lett. **106**, 186601 (2011).

[37]M. Costache, G. Bridoux, I. Neumann, and S. Valenzuela, "Magnon-drag thermopile," Nature Mater. **11**, 199 (2012).

[38]I. Terasaki, "High-temperature oxide thermoelectric," J. Appl. Phys. **110**, 053705 (2011).

[39]L. Karvonen, P. Tomes, and A. Weidenkaff, "Thermoelectric performance of perovskite-type oxide materials," Material Matters **6**(4), 92 (2011). Available at http://www.sigmaaldrich.com/technical-documents/articles/material-matters/perovskite-type-oxide-materials.html.